Similarity solution of fuel mass transfer, port mass flux coupling in hybrid propulsion

B. J. Cantwell

Journal of Engineering Mathematics

ISSN 0022-0833

J Eng Math
DOI 10.1007/s10665-013-9624-y

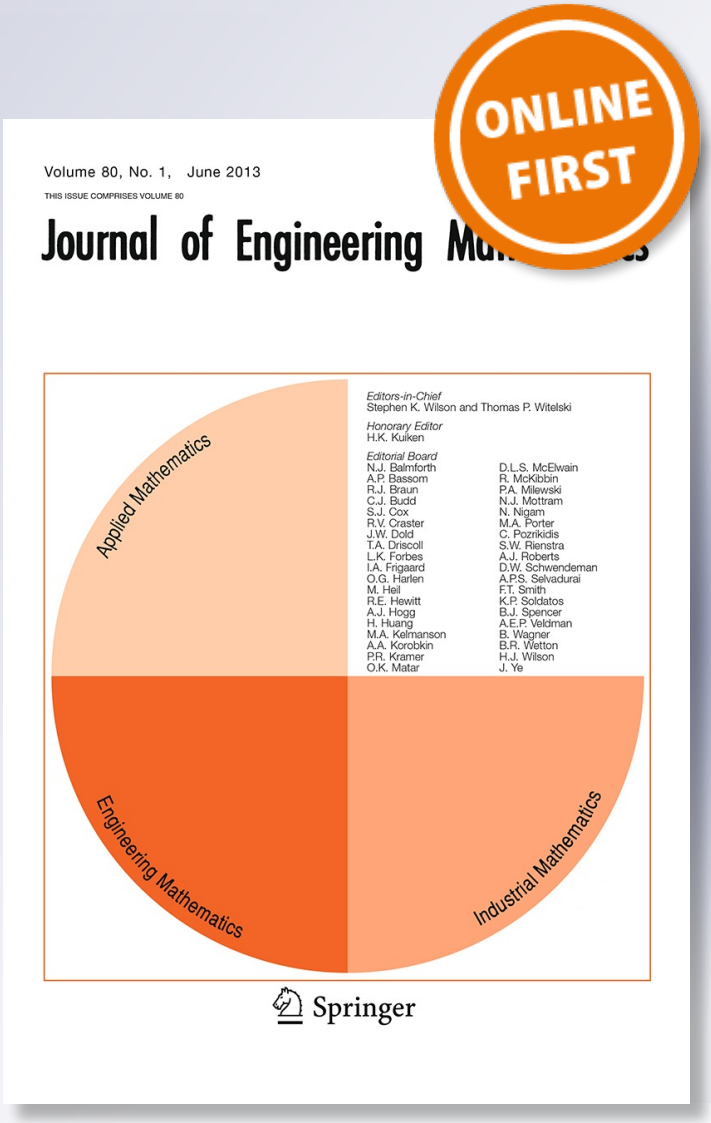

Springer

J Eng Math
DOI 10.1007/s10665-013-9624-y

Similarity solution of fuel mass transfer, port mass flux coupling in hybrid propulsion

B. J. Cantwell

Received: 30 August 2012 / Accepted: 21 January 2013

Abstract Boundary layer combustion is the primary mechanism of hot gas generation in hybrid rockets. The idea of a hybrid rocket is to store the oxidizer as a liquid and the fuel as a solid, producing a design that is less susceptible to chemical explosion than conventional solid and bipropellant liquid designs. The fuel is contained within the rocket combustion chamber in the form of a cylinder, with a circular channel called a port hollowed out along its axis. Upon ignition, a diffusion flame forms over the fuel surface along the length of the port. The combustion is sustained by heat transfer from the flame to the solid fuel causing continuous fuel vaporization until the oxidizer flow is turned off. Theory shows that the fuel mass transfer rate is proportional to the mass flux averaged across the port. The mass flow rate increases with axial distance, leading to coupling between the local fuel regression rate and the local mass flux. For proper design, accurate expressions are needed for both the time-dependent oxidizer-to-fuel ratio at the end of the port and the time at which all the fuel is consumed. As the fuel is depleted, the flame approaches the motor case, at which point the burn must be terminated. The purpose of this paper is to present a similarity solution for the coupled problem and a brief discussion of current practice.

Keywords Combustion · Propulsion · Hybrid rocket · Paraffin · Regression rate · Fuel · Oxidizer · Lie group · Similarity solution · Phase portrait

1 Introduction

When I first came to Stanford as an assistant professor in 1978, Milton Van Dyke graciously asked me to coteach his course on similitude. This was a wonderful opportunity to learn from one of the great teachers of fluid mechanics. That collaboration and the lifelong friendship that followed formed the basis of the course I teach today at Stanford. The problem I treat in this paper uses dimensional analysis (one of Milt's favorite tools) to analyze the coupling between mass transfer and mass flux in a reacting flow in a circular cross-section channel.

This paper is dedicated to the memory of Milton Van Dyke, whose life and work inspired generations of students and researchers throughout the world.

B. J. Cantwell (✉)
Department of Aeronautics and Astronautics, Stanford University, Stanford, CA 94305, USA
e-mail: cantwell@stanford.edu

Published online: 25 June 2013

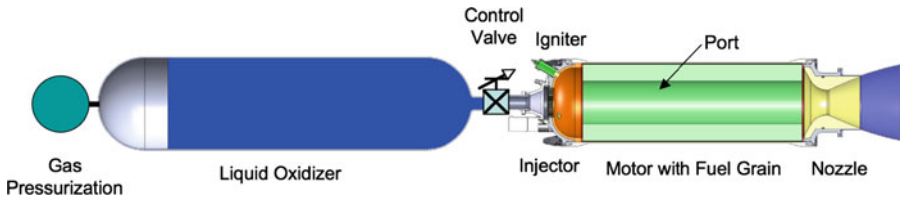

Fig. 1 Single-port hybrid rocket cross section

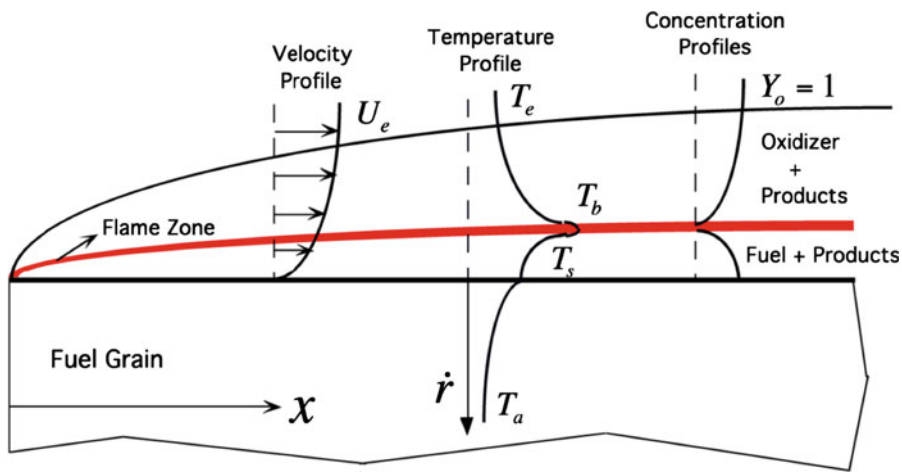

Fig. 2 Boundary layer combustion

The hazardous operation of the two basic types of chemical rocket propulsion comes mainly from the oxidizer and fuel that must be mixed to release energy in the rocket combustion chamber. In liquid bipropellant rockets, a pump leak or tank rupture that brings these chemicals together in an uncontrolled way can result in a large explosion. In solid propellant rockets, the fuel and oxidizer are premixed and held together in a polymer binder. Cracks or imperfections in the propellant can cause uncontrolled combustion and explosion. The idea of a hybrid rocket is to store the oxidizer as a liquid and the fuel as a solid. Uncontrolled mixing of fuel and oxidizer cannot occur, making the hybrid much less susceptible to chemical explosion than conventional systems. The fuel is contained within the rocket combustion chamber in the form of a cylindrical grain, with one or more ports. Figure 1 illustrates a single-port design.

Chiaverini and Kuo [1] provide a comprehensive discussion of the fundamentals of hybrid rocket operation. Combustion takes place through diffusive mixing between vaporized oxidizer flowing through the port and fuel evaporating from the solid surface. The idealized sketch in Fig. 2 illustrates the flow configuration. The flame thickness and location in the boundary layer are shown roughly to scale. The flame zone is relatively deep in the boundary layer and, according to Marxman and Gilbert [2] and Marxman et al. [3], the flame tends to be fuel rich based on the observed flame position and relatively low flame temperatures measured in the boundary layer.

The hybrid enjoys many safety and environmental advantages over conventional systems; however, large hybrids have not been commercially successful. The reason is that traditional systems use polymeric fuels that evaporate too slowly, making it difficult to produce the high thrust needed for most applications. A low regression rate has to be compensated by increasing the burning surface area, leading to a complex multiport port design that compromises motor performance. Figure 3 shows a sketch of what would be called a wagon wheel design.

Research at Stanford University in the late 1990s by Karabeyoglu et al. [4] led to the identification of solid paraffin fuels that burn at regression rates three to four times faster than polymeric fuels. Heat transfer from the combustion zone and the action of the gas flow over the melting fuel surface leads to the formation of a thin, hydrodynamically unstable liquid film. Karabeyoglu and Cantwell [5] used boundary conditions from Benjamin [6]

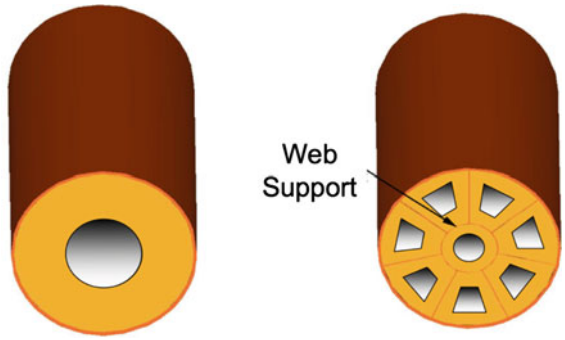

Fig. 3 Single-port versus multiport design

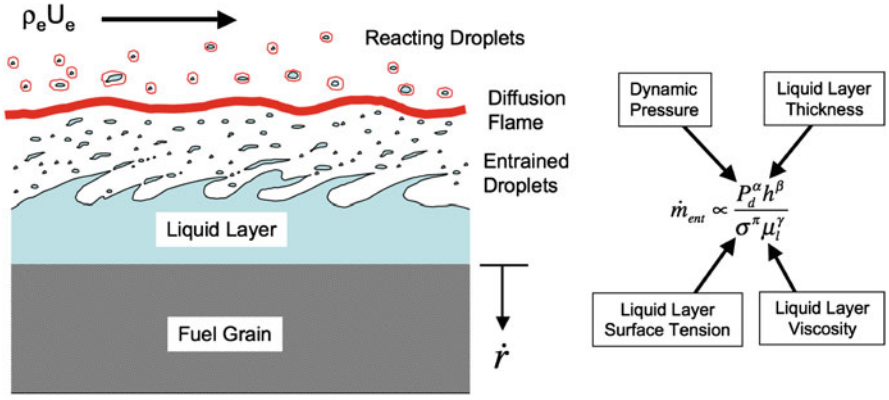

Fig. 4 Liquid layer instability mechanism and entrainment mass transfer correlation

to extend the theory of Craik [7] and show that the liquid–gas interface is linearly unstable under the flow conditions found in hybrid rockets. To treat the nonlinear problem, an empirical mass transfer correlation was developed using the data of Gater and L'Ecuyer [8]. The model showed that for paraffin the low viscosity of the liquid layer leads to entrainment of droplets from the liquid–gas interface, as illustrated in Fig. 4 from Cantwell et al. [9]. This mechanism substantially increases the rate of fuel mass transfer, leading to a much higher regression rate than can be achieved with conventional polymeric fuels by a factor of three to five. In the past decade this advance has led to renewed interest in hybrids as a low-cost alternative to conventional systems.

The fuel surface regression rate, $\dot{r}$, where r is the radius of the port, generally follows the classical theory developed by Marxman and Gilbert [2] and Marxman [10]. The regression rate is governed by turbulent heat and mass transfer in the reacting boundary layer. In the development of the theory, the Lewis number and turbulent Prandtl number are assumed to be one. Radiative heat transfer effects can be shown to be relatively small and are neglected. In addition, the Reynolds analogy between heat transfer and skin friction is assumed to hold, and a power-law form of the turbulent boundary layer velocity profile is used.

In practice, the most widely used form of the regression rate law that has proven to be accurate over a substantial range of propellant combinations and scales is

$$\dot{r} = a\frac{G^n}{x^m}, \tag{1}$$

where G is the local mass flux in the port,

$$G = \frac{\dot{m}_{\text{port}}}{\pi r^2} = \frac{\dot{m}_{\text{ox}} + \dot{m}_{\text{f}}}{\pi r^2}. \tag{2}$$

The local port mass flow rate, $\dot{m}_{\text{port}}$, is composed of the oxidizer mass flow rate, $\dot{m}_{\text{ox}}$, injected at the entrance to the port, and the accumulated fuel mass flow rate, $\dot{m}_{\text{f}}$, transferred from the fuel grain upstream of a location x. The

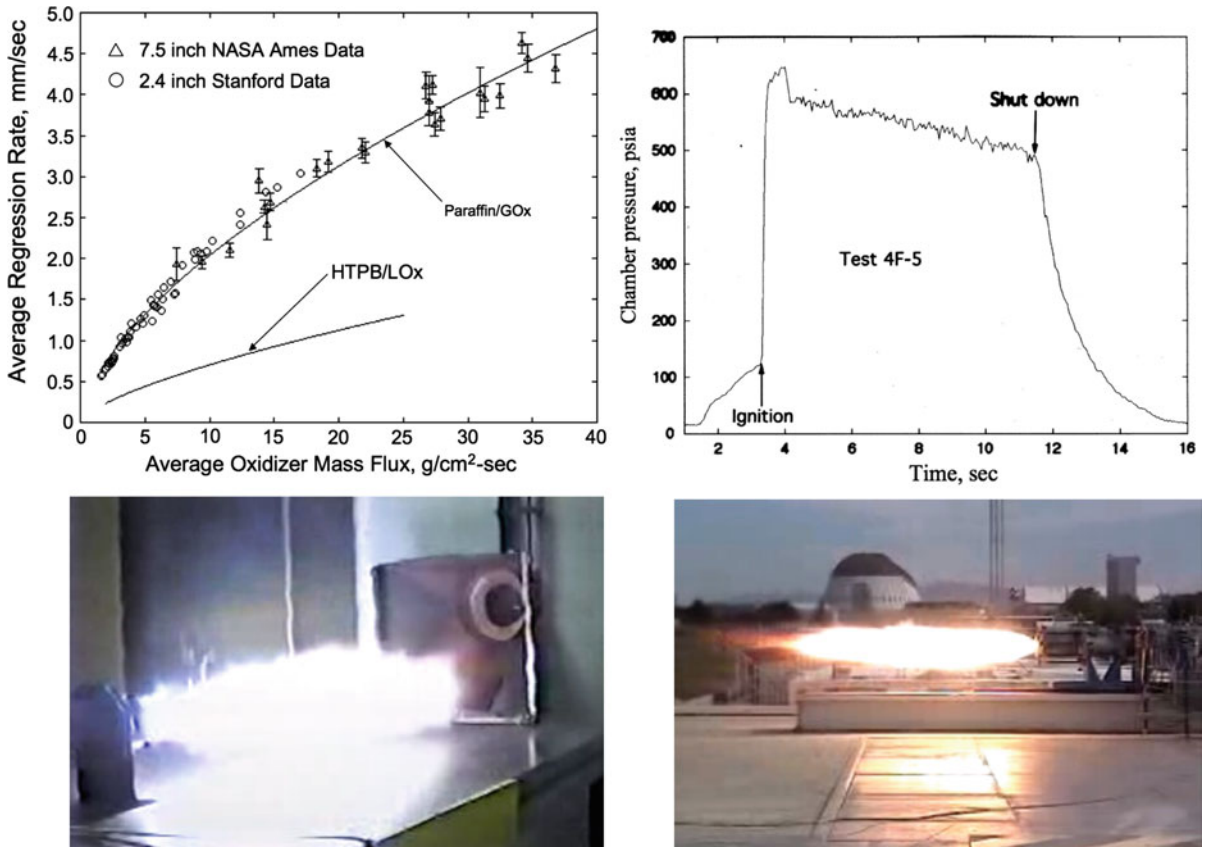

Fig. 5 Regression rate data for paraffin fuel burning wih gaseous oxygen. The figure on the *upper right* shows the chamber pressure versus time history for a typical test. Images are from a 200 N thrust test at Stanford and a 3000 N thrust test at NASA Ames

coefficient a is an empirical constant determined by the choice of fuel and oxidizer. The units of the regression rate constant

$$[a] = \frac{\text{Length}^{2n+m+1}}{\text{Mass}^{n}\text{Time}^{1-n}} \tag{3}$$

will play a central role in the analysis developed in this paper. The dependence of regression rate on mass flux G and streamwise coordinate x arises from the dependence of the skin friction and heat transfer rate on the Reynolds number based on the distance along the port. The classical values of the exponents suggested by Marxman's theory are $m = 0.2$ and $n = 1 - m = 0.8$. Measured values of n tend to be in the range 0.3–0.8 depending on the choice of fuel and oxidizer. Values of n greater than 0.8 or less than approximately 0.3 are not observed. The length exponent turns out to be very difficult to measure since it is relatively small and would require a large number of motor tests at a wide range of scales to be determined accurately. As nearly as one can tell at this point m is considerably smaller than the predictions of classical theory.

Figure 5 shows results from an extensive set of tests carried out at Stanford University and NASA Ames Research Center by Karabeyoglu et al. [11]. Four selected cases were analyzed by Karabeyoglu et al. [12]. The results for a paraffin-based fuel burning with gaseous oxygen gave $n = 0.62$. The measured values of m for the four cases were 0, 0.009, 0.018, and 0.033, with an average value of 0.015. The corresponding values of a were 9.36×10^{-5}, 9.24×10^{-5}, 9.36×10^{-5}, and 9.10×10^{-5}, with an average of 9.27×10^{-5}, where the mass flux is measured in $\text{kg}/(\text{m}^2\,\text{s})$, the port length is in meters, and the regression rate is in meters per second. The question of the length exponent is an important one since it determines the dependence of the fuel regression rate on the size of the motor and the limiting motor size that can be designed with just a single circular port.

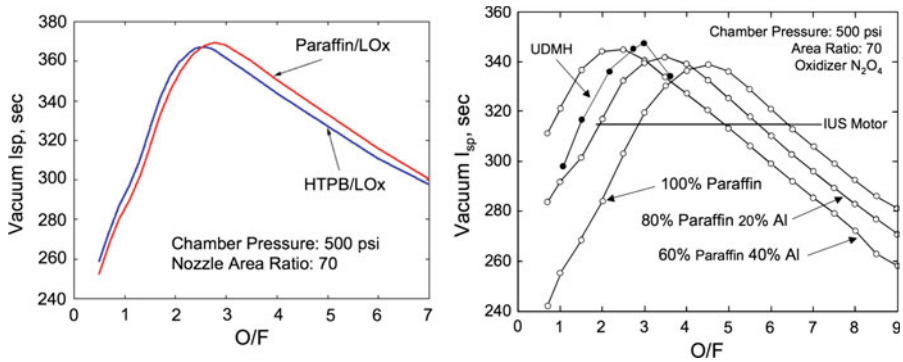

Fig. 6 **a** Ideal specific impulse for paraffin and HTPB burning with LOx. **b** Paraffin-aluminum mixtures burning with nitrogen tetroxide. The IUS (inertial upper stage) motor was a solid rocket built by the Chemical Systems Division of United Technologies and used as an upper stage in Boeing satellite launches for many years

The remarkable set of data measured by Wooldridge and Muzzy [13] on wall injection with and without heating generally supports Marxman's model. Paul et al. [14] modified Marxman's theory in an attempt to more accurately include the molecular weight variation across the boundary layer due to pyrolysis of high-molecular-weight polymeric fuels such as hydroxyl-terminated polybutadiene (HTPB).

In marked contrast to solid rockets, the regression rate of a hybrid is insensitive to the chamber pressure except at very low fluxes where radiation effects become important and at very high fluxes where chemical kinetics effects are important. This key advantage of hybrids enables the designer to optimize the chamber pressure for a given mission. In a solid rocket, the flame is much closer to the fuel surface and the regression rate is typically an order of magnitude larger.

The theoretical specific impulse of a hybrid rocket is more appropriately compared to a bipropellant liquid than a solid. This is because the oxidizers are the same and the solid fuels are generally hydrocarbons with energy content similar to that of kerosene. However, hybrid solid fuel densities are typically 15–20 % greater than the density of liquid kerosene. Figure 6 depicts the theoretical specific impulse versus oxidizer-to-fuel(O/F) ratio of liquid oxygen (LOx) burning with paraffin and HTPB, a common solid propellant binder. The plot on the right shows paraffin burning with N_2O_4 with varying percentages of aluminum added to the fuel by mass. Aluminum addition tends to increase the specific impulse slightly while reducing the optimal O/F, allowing the designer to use a smaller liquid storage and feed system. These figures give a pretty good illustration of the range of the O/F ratio used in typical systems. The main point is that the oxidizer mass flow rate tends to be two or more times the fuel mass flow rate at the end of the port.

Over the course of a burn at a fixed oxidizer mass flow rate, there is a tendency for the oxidizer-to-fuel (O/F) ratio to shift to higher values as the port opens up. This can be seen from what follows. At the end of a straight circular port,

$$O/F = \frac{\dot{m}_{\rm ox}}{\dot{m}_{\rm f}} = \frac{\dot{m}_{\rm ox}}{\rho_f A_b \dot{r}} = \frac{\dot{m}_{\rm ox}}{2\rho_f L_{\rm port}\pi r a \left(\frac{\dot{m}_{\rm ox}}{\pi r^2}\right)^n} = \frac{\dot{m}_{\rm ox}^{1-n} r^{2n-1}}{2\pi^{1-n} a \rho_f L_{\rm port}}, \tag{4}$$

where the fuel mass flow rate in (2) is neglected compared to $\dot{m}_{\rm ox}$ and the length exponent is taken to be $m = 0$. The quantity ρ_f is the fuel density, A_b is the port surface area, and $L_{\rm port}$ is the length of the port. The fuel mass flow rate, $\dot{m}_{\rm f}$, is calculated assuming that the port radius is constant along its axis. Recall that the exponent is generally in the range $0.3 < n < 0.8$. As the port diameter increases, the burning area increases and the oxidizer mass flux goes down. For $n > 0.5$ the decrease in mass flux dominates the increase in port surface area and the overall fuel mass flow rate goes down. The net effect is to cause the chamber pressure, and hence the thrust, to decrease naturally over the course of the burn as the vehicle mass decreases. This feature is desirable for a launch system where the payload is subject to a maximum acceleration constraint. Compare this to a solid rocket where the propellant regression rate increases with chamber pressure and the thrust tends to increase during the burn. Furthermore, in a solid rocket a

throttling option is generally not available, requiring a complex port design to prevent excessive acceleration of the payload.

Note that the O/F shift implied by Eq. (4) means that the specific impulse cannot be maintained at its peak value at a constant oxidizer mass flow rate. Figure 3 shows that for oxygen burning with paraffin or HTPB, for which $n > 0.5$, the performance can drop off quite steeply as the O/F ratio moves away from the value corresponding to peak I_{sp}. The change in the O/F ratio with the opening up of the port implies a change in specific impulse and a possible reduction in vehicle performance. This factor must be taken into account by the designer seeking to attain maximum total delivered impulse from the motor. In reality, the exponent $2n - 1$ is quite small, and if one designs the hybrid to begin burning at an O/F somewhat to the left of peak I_{sp} and finish burning at an O/F slightly above the peak, then the loss of total delivered impulse can be kept to a few percent or less depending on the oxidizer. Generally, the maximum payload acceleration limit leads to the requirement that the oxidizer mass flow rate must be throttled back while the port opens up, and the two effects tend to offset one another. For nitrous oxide (N_2O) burning with paraffin, the exponent turns out to be very close to 0.5, and the O/F shift due to the opening up of the port is negligible.

Throttling over a wide range is another matter. According to Eq. (4), the dependence of the O/F ratio on the oxidizer mass flow rate is fairly strong. With oxygen, large O/F and, hence, large I_{sp} variations do occur. This consideration can lead the designer to select a nitrogen-based oxidizer, such as N_2O or N_2O_4, for which the sensitivity of I_{sp} to O/F near the peak I_{sp} is considerably less than that of LOx. This choice would have to be balanced with the loss of I_{sp}, the relative increase in oxidizer total mass, and the increased size of the liquid storage and delivery system.

In Sect. 2 a solution to the simplified form of the regression rate law is described, and this is followed in Sect. 3 by the formulation of the full fuel mass transfer, port mass flux coupled problem. In Sect. 4 an exact solution of the coupled problem is described for $n = 1/2$. The group invariance of the coupled problem is treated in Sect. 5, along with the construction of similarity variables and the reduction of the problem to an autonomous pair of ordinary differential equations (ODEs). The analytical/numerical solution of this system, appropriate to the hybrid rocket problem, is described in detail in Sects. 6–9. In Sect. 10 the solution is applied to dimensionless examples for $n > 1/2$ and $n < 1/2$. Scaling issues are discussed in Sect. 11, and the solution is applied to two dimensioned examples and compared to measured data. The agreement with the data is excellent, confirming the relevance of the similarity solution to motor test data. Section 12 contains concluding remarks and some discussion of the road forward.

2 Port radius solution neglecting the effect of fuel mass flow on regression rate

The simplest approach to determining how the port radius varies with time is to neglect the effect of accumulated fuel mass flow on the regression rate in (2) and assume the length exponent $m = 0$ so the port radius is independent of x. This utilizes the fact that m is known to be small, allowing the singularity at $x = 0$ to be removed. Moreover, the optimal O/F is often three or more, so the oxidizer usually comprises most of the mass flow in the port. It is a common assumption that can easily be replaced using the similarity solution derived in what follows. Integrate (1):

$$\frac{\mathrm{d}r(t)}{\mathrm{d}t} = a\left(\frac{\dot{m}_{\mathrm{ox}}(t)}{\pi r^2}\right)^n, \tag{5}$$

$$r(t) = \left(r(0)^{2n+1} + (2n+1)\,\frac{a}{\pi^n}\int_0^t \dot{m}_{\mathrm{ox}}(t')^n \mathrm{d}t'\right)^{\frac{1}{2n+1}}. \tag{6}$$

In this case, the mass flow simply increases linearly along the port:

$$\frac{\dot{m}_{\mathrm{port}}}{\dot{m}_{\mathrm{ox}}} = \frac{\dot{m}_{\mathrm{f}} + \dot{m}_{\mathrm{ox}}}{\dot{m}_{\mathrm{ox}}} = 1 + \frac{2\pi^{1-n} a \rho_f x}{\dot{m}_{\mathrm{ox}}^{1-n}\left(r(0)^{2n+1} + (2n+1)\,\frac{a}{\pi^n}\int_0^t \dot{m}_{\mathrm{ox}}(t')^n \mathrm{d}t'\right)^{\frac{2n-1}{2n+1}}}. \tag{7}$$

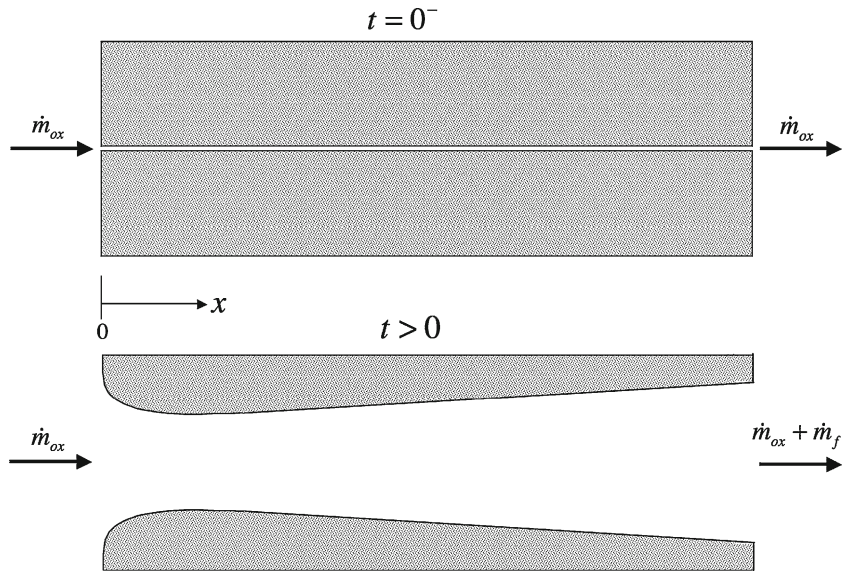

Fig. 7 Problem formulation showing grain initial condition and typical port shape after some burn time has elapsed

3 Coupled space–time formulation

In reality, the regression rate is dependent on the local total mass flux including the fuel mass accumulated along the port, and in turn the local mass flux depends on the local radius. The problem is governed by two coupled first-order partial differential equations (PDEs), the regression rate equation

$$\frac{\partial r(x,t)}{\partial t} = \pi^{-n} a \frac{\dot{m}_{\text{port}}^n}{x^m r^{2n}} \tag{8}$$

and the mass flow growth equation

$$\frac{\partial \dot{m}_{\text{port}}(x,t)}{\partial x} = 2\pi^{1-n} a \rho_f \frac{\dot{m}_{\text{port}}^n}{x^m r^{2n-1}}. \tag{9}$$

Equation (9) comes from the balance between the local rate of change of mass flow and the outward movement of the port radius governed by the mass generation compatibility equation

$$\frac{\partial \dot{m}_{\text{port}}}{\partial x} = 2\pi \rho_f r \frac{\partial r}{\partial t}. \tag{10}$$

This problem was studied in detail by Karabeyoglu et al. [12], who included a numerical solution of (8) and (9) for the paraffin/oxygen data measured at NASA Ames and described in the introduction. In the present paper I would like to reexamine this problem in light of a new similarity solution of (8) and (9). The problem formulation is shown in Fig. 7.

Just prior to $t = 0$ the oxidizer mass flow is established all along the port, which is assumed to have an initial radius of $r(x, 0) = 0$. The oxidizer mass flow, $\dot{m}_{\text{ox}}$, entering the port is a prescribed function of time, $\dot{m}_{\text{port}}(0, t) = \dot{m}_{\text{ox}}(t)$. For $t > 0$ fuel mass transfer occurs and the port opens up.

4 Exact solution for $n = 1/2$ and time-dependent $\dot{m}_{\text{ox}}$

Karabeyoglu et al. (2005) provide the exact solution of (8) and (9) for $n = 1/2$. In this case the equations simplify to

$$\frac{\partial}{\partial t}\left(r^2\right) = 2\pi^{-1/2} a \frac{\dot{m}_{\text{port}}^{1/2}}{x^m} \tag{11}$$

and

$$\frac{\partial \dot{m}_{\text{port}}}{\partial x} = 2\pi^{1/2} a \rho_f \frac{\dot{m}_{\text{port}}^{1/2}}{x^m} \tag{12}$$

with the solution

$$\dot{m}_{\text{port}}(x,t) = \left(\dot{m}_{\text{ox}}(t)^{1/2} + \frac{\pi^{1/2} a \rho_f x^{1-m}}{1-m} \right)^2 \tag{13}$$

and

$$r(x,t) = \left(r(0,t)^2 + \frac{2\pi^{-1/2} a}{x^m} \left\{ \int_0^t \dot{m}_{\text{ox}}(t')^{1/2} \mathrm{d}t' + \frac{\pi^{1/2} a \rho_f x^{1-m} t}{1-m} \right\} \right)^{1/2}. \tag{14}$$

The $n = 1/2$ solution can encompass an initial radius $r(0,t)$ that is nonzero. For $n = 1/2$ the increased fuel mass generation due to the increase in port surface area is exactly compensated by the decrease in mass flux due to the growth in port cross-sectional area. As a result, the total mass flow rate (13) at any point in the port is independent of time if $\dot{m}_{\text{ox}}$ is constant. For $n > 1/2$ the effect of decreasing mass flux dominates the increase in port surface area and the mass flow at a given coordinate x decreases with time as the port opens up. If $n < 1/2$, then the mass flow increases with time.

5 Similarity formulation, constant $\dot{m}_{\text{ox}}$, reduction to an autonomous system

The parameters governing the problem with their units are

$$\begin{aligned} &\left[2\pi\rho_f\right] = \text{Mass/Length}^3, \\ &\left[\dot{m}_{\text{ox}}\right] = \text{Mass/Time}, \\ &\left[\pi^{-n} a\right] = \text{Mass}^{-n}\text{Length}^{2n+m+1}\text{Time}^{n-1}, \end{aligned} \tag{15}$$

where the factors of π are included for convenience. These parameters can be used to determine characteristic mass, length, and time scales for the problem:

$$\begin{aligned} T_{\text{ch}} &= \left[\frac{(\dot{m}_{\text{ox}})^{\frac{1-n+m}{2-2n-m}}}{\left(\pi^{-n} a\right)^{\frac{3}{2-2n-m}} \left(2\pi\rho_f\right)^{\frac{1+2n+m}{2-2n-m}}} \right], \\ L_{\text{ch}} &= \left[\frac{(\dot{m}_{\text{ox}})^{\frac{1-n}{2-2n-m}}}{\left(\pi^{-n} a\right)^{\frac{1}{2-2n-m}} \left(2\pi\rho_f\right)^{\frac{1}{2-2n-m}}} \right], \\ M_{\text{ch}} &= \left[\frac{(\dot{m}_{\text{ox}})^{\frac{3-3n}{2-2n-m}}}{\left(\pi^{-n} a\right)^{\frac{3}{2-2n-m}} \left(2\pi\rho_f\right)^{\frac{1+2n+m}{2-2n-m}}} \right]. \end{aligned} \tag{16}$$

These scales are used to nondimensionalize the variables and equations as follows:

$$\chi = \frac{x}{L_{\text{ch}}}, \quad \tau = \frac{t}{T_{\text{ch}}}, \quad R = \frac{r}{L_{\text{ch}}}, \quad J = \frac{\dot{m}_{\text{port}}}{\dot{m}_{\text{ox}}}. \tag{17}$$

A key design variable is the O/F ratio of the motor:

$$O/F = \frac{\dot{m}_{\text{ox}}}{\dot{m}_f} = \frac{1}{J-1}. \tag{18}$$

In dimensionless form, the equations governing the port flow are

$$\frac{\partial R(\chi,\tau)}{\partial \tau} = \frac{J^n}{\chi^m R^{2n}} \tag{19}$$

and

$$\frac{\partial J(\chi,\tau)}{\partial \chi} = \frac{J^n}{\chi^m R^{2n-1}}. \tag{20}$$

The partial derivatives are related by the compatibility Eq. (10)

$$\frac{\partial J}{\partial \chi} = \frac{\partial}{\partial \tau}\left(\frac{R^2}{2}\right). \tag{21}$$

In dimensionless form, the initial conditions of the problem are

$$R(\chi,0) = 0, \quad J(0,\tau) = 1. \tag{22}$$

In these variables, the constant port radius solution (6) and (7) is

$$R = ((2n+1)\,\tau)^{\frac{1}{2n+1}}, \quad J = 1 + \frac{\chi}{((2n+1)\,\tau)^{\frac{2n-1}{2n+1}}}. \tag{23}$$

Similarly, Eqs. (13) and (14), the exact solution for $n = 1/2$, are

$$R = \left(\frac{2\tau}{\chi^m}\right)^{\frac{1}{2}}\left(1 + \frac{\chi^{1-m}}{2(1-m)}\right)^{\frac{1}{2}}, \quad J = \left(1 + \frac{\chi^{1-m}}{2(1-m)}\right)^2. \tag{24}$$

Both (23) and (24) are for constant $\dot{m}_{\mathrm{ox}}$.

We can use symmetry methods to carry out a reduction of the system (19) and (20). These techniques are well described in Olver [15], Bluman and Kumei [16], Ibragimov [17], and Cantwell [18]. Equations (19) and (20) admit a three-dimensional Lie algebra with infinitesimal group operators

$$\begin{aligned} X^a &= \frac{\partial}{\partial \tau}, \\ X^b &= \left(\frac{1-n}{1-m}\right)\chi\frac{\partial}{\partial \chi} - \left(\frac{n-m}{1-m}\right)\tau\frac{\partial}{\partial \tau} + J\frac{\partial}{\partial J}, \\ X^c &= \chi\frac{\partial}{\partial \chi} + \left(\frac{2n-2m+1}{2n-1}\right)\tau\frac{\partial}{\partial \tau} + \left(\frac{1-m}{2n-1}\right)R\frac{\partial}{\partial R}. \end{aligned} \tag{25}$$

The translation group in time, X^a, can be used to define time with respect to flow initiation at $t = t_0$. There is really nothing gained by doing this for this problem, and so $t_0 = 0$ will be used. The dilation group, X^b, would govern a self-similar problem in which the port radius at the boundary is held fixed while the oxidizer mass flow is increased with time from zero; this is not the problem we wish to solve.

The finite transformation corresponding to the second dilation group with operator X^c and group parameter c is

$$\begin{aligned} \tilde{\chi} &= \mathrm{e}^c\chi, \\ \tilde{\tau} &= \mathrm{e}^{\frac{2n-2m+1}{2n-1}c}\tau, \\ \tilde{R} &= \mathrm{e}^{\frac{1-m}{2n-1}c}R, \\ \tilde{J} &= J. \end{aligned} \tag{26}$$

The boundary curves of the problem and the boundary conditions are invariant under (26):

$$\begin{aligned} &0 < \tilde{\chi} < \infty \Rightarrow 0 < \mathrm{e}^c\chi < \infty && \Rightarrow \quad 0 < \chi < \infty, \\ &0 < \tilde{\tau} < \infty \Rightarrow 0 < \mathrm{e}^{\frac{2n-2m+1}{2n-1}c}\tau < \infty && \Rightarrow \quad 0 < \tau < \infty, \\ &0 < \tilde{R} < \infty \Rightarrow 0 < \mathrm{e}^{\frac{1-m}{2n-1}c}R < \infty && \Rightarrow \quad 0 < R < \infty, \\ &\tilde{R}(\tilde{\chi},0) = 0 \Rightarrow \mathrm{e}^{\frac{1-m}{2n-1}c}R(\mathrm{e}^c\chi,0) = 0 && \Rightarrow \quad R(\chi,0) = 0, \\ &\tilde{J}(0,\tilde{\tau}) = 1 \Rightarrow J\left(0, \mathrm{e}^{\frac{2n-2m+1}{2n-1}c}\tau\right) = 1 && \Rightarrow \quad J\,(0,\tau) = 1. \end{aligned} \tag{27}$$

The invariance of J in dilation group (26) preserves the boundary condition $J(0,\tau) = 1$. The invariance of the governing equations and boundary functions is essentially a proof of the existence of a similarity solution to the problem that is also invariant under (26). The characteristic equations of X^c ,

$$\frac{\mathrm{d}\chi}{\chi} = \frac{\mathrm{d}\tau}{\left(\frac{2n-2m+1}{2n-1}\right)\tau} = \frac{\mathrm{d}R}{\left(\frac{1-m}{2n-1}\right)R} = \frac{\mathrm{d}J}{0}, \tag{28}$$

are integrated to generate the similarity variables

$$\theta = \frac{\chi}{\tau^{\left(\frac{2n-1}{2n-2m+1}\right)}}, \quad K(\theta) = \frac{R}{\chi^{\left(\frac{1-m}{2n-1}\right)}}, \quad J(\theta) = J. \tag{29}$$

Substituting (29) into (19) and (20) leads to a pair of ODEs in the similarity variable θ:

$$K_\theta = -\left(\frac{2n-2m+1}{2n-1}\right)\frac{J^n}{\theta^{\left(\frac{4n-2m}{2n-1}\right)}K^{2n}} \tag{30}$$

and

$$J_\theta = \frac{J^n}{\theta K^{2n-1}} \tag{31}$$

with boundary conditions

$$K(\infty) = 0, \quad J(0) = 1. \tag{32}$$

The compatibility relation (21) becomes

$$J_\theta = -\left(\frac{2n-1}{2n-2m+1}\right)\theta^{\left(\frac{2n-2m+1}{2n-1}\right)}\left(\frac{K^2}{2}\right)_\theta. \tag{33}$$

System (30) and (31) is invariant under the one-parameter dilation group

$$\begin{aligned}\tilde{\theta} &= \mathrm{e}^a\theta,\\ \tilde{K} &= \mathrm{e}^{-(1-n)\left(\frac{2n-2m+1}{2n-1}\right)a}K,\\ \tilde{J} &= \mathrm{e}^{(2n-2m+1)a}J.\end{aligned} \tag{34}$$

We can use this group to reduce (30) and (31) to an autonomous system. The characteristic equations of (34)

$$\frac{\mathrm{d}\theta}{\theta} = \frac{\mathrm{d}K}{-(1-n)\left(\frac{2n-2m+1}{2n-1}\right)K} = \frac{\mathrm{d}J}{(2n-2m+1)J} \tag{35}$$

lead to new dependent variables

$$u(\theta) = \frac{1}{\theta^{(1-n)\left(\frac{2n-2m+1}{2n-1}\right)}K(\theta)}, \quad v(\theta) = \frac{\theta^{2n-2m+1}}{J(\theta)}. \tag{36}$$

The inverse choice of the variables here is used because it will later simplify the interpretation of the system phase portrait. Upon substitution of (36) into (30) and (31) the governing equations reduce to the autonomous pair

$$\frac{\mathrm{d}u}{\mathrm{d}\alpha} = \left(\frac{1-n}{2n-1}\right)\left(\frac{1}{(1-n)}u^{2n+2}v^{-n} - u\right) \tag{37}$$

and

$$\frac{\mathrm{d}v}{\mathrm{d}\alpha} = \left(v - \frac{1}{(2n-2m+1)}v^{2-n}u^{2n-1}\right), \tag{38}$$

where

$$\alpha = (2n-2m+1)\,\mathrm{Log}(\theta). \tag{39}$$

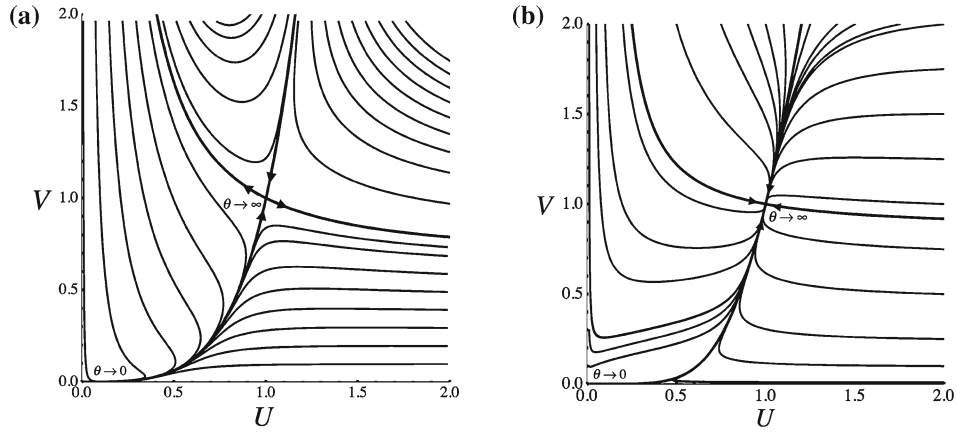

Fig. 8 Phase portrait of (43) and (44). **a** Figure shows the Saddle point for $n = 0.8$. **b** Figure shows the Stable node for $n = 0.3$

In these variables the compatability relation (33) is

$$\frac{1}{u^2} + \left(\frac{2n-1}{1-n}\right)\frac{1}{u^3}\frac{\mathrm{d}u}{\mathrm{d}\alpha} = \left(\frac{2n-2m+1}{1-n}\right)\frac{1}{v} - \left(\frac{2n-2m+1}{1-n}\right)\frac{1}{v^2}\frac{\mathrm{d}v}{\mathrm{d}\alpha}. \tag{40}$$

Equations (37) and (38) have two critical points, a nonlinear unstable node at $(u, v) = (0, 0)$ and a linear saddle point (or node) at

$$(u_c, v_c) = \left((2n-2m+1)^n\,(1-n)^{1-n}\,, \frac{(2n-2m+1)^{2n+1}}{(1-n)^{(2n-1)}}\right). \tag{41}$$

In the following analysis it will be useful to normalize (37) and (38) using the coordinates of the critical point at (41). Let

$$U = \frac{u}{u_c}, \quad V = \frac{v}{v_c}. \tag{42}$$

In these variables the governing equations become

$$\frac{\mathrm{d}U}{\mathrm{d}\alpha} = \left(\frac{1-n}{2n-1}\right)U\left(\frac{U^{2n+1}}{V^n} - 1\right) \tag{43}$$

and

$$\frac{\mathrm{d}V}{\mathrm{d}\alpha} = V\left(1 - \left(\frac{V}{U^2}\right)\frac{U^{2n+1}}{V^n}\right), \tag{44}$$

and the compatibility condition is

$$\left(\frac{1}{U^2} + \left(\frac{2n-1}{1-n}\right)\frac{1}{U^3}\frac{\mathrm{d}U}{\mathrm{d}\alpha}\right) = \left(\frac{1}{V} - \frac{1}{V^2}\frac{\mathrm{d}V}{\mathrm{d}\alpha}\right). \tag{45}$$

The first-order ODE governing $V(U)$ is

$$\frac{\mathrm{d}V}{\mathrm{d}U} = \left(\frac{2n-1}{1-n}\right)\frac{V}{U}\frac{\left(1 - \left(\frac{V}{U^2}\right)\frac{U^{2n+1}}{V^n}\right)}{\left(\frac{U^{2n+1}}{V^n} - 1\right)}. \tag{46}$$

The phase portrait of (43) and (44) is shown in Fig. 8 for values above and below $n = 1/2$.

Note that when system (37) and (38) is expressed in variables normalized by the critical point coordinates, the phase portrait is independent of the length exponent m. The eigenvalues of (43) and (44) near the critical point $(U, V) = (1, 1)$ satisfy

$$\lambda^2 + P\lambda + Q = 0, \tag{47}$$

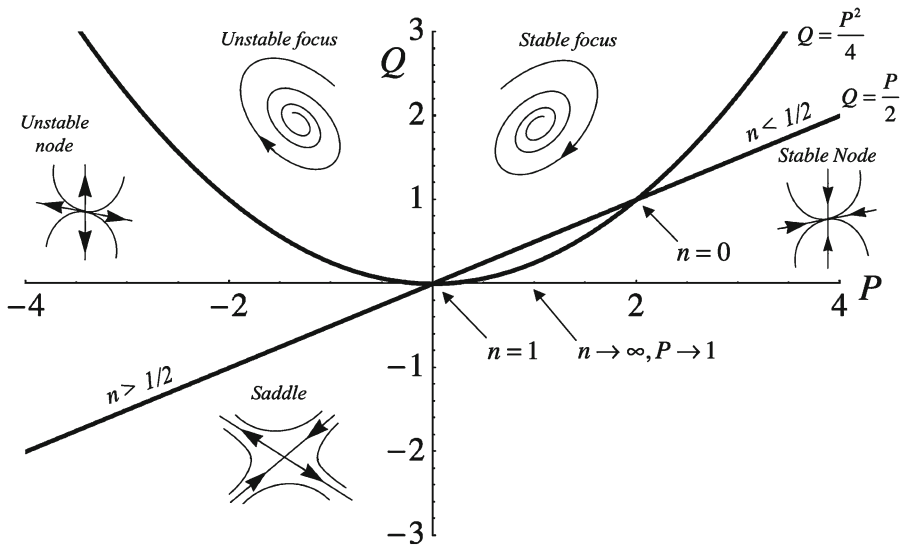

Fig. 9 Cross plot of critical point invariants. A critical point is a saddle if $1/2 < n < 1$ and a stable node for $0 < n < 1/2$

where the invariants are

$$P = -2\left(\frac{1-n}{2n-1}\right) \tag{48}$$

and

$$Q = -\left(\frac{1-n}{2n-1}\right) = \frac{P}{2}. \tag{49}$$

In Fig. 9 various possibilities for the critical point are shown in the overlay of (49) with the cross plot of invariants. The solution that concerns us lies on the branch that connects the critical point to the origin, as indicated by the limiting values of θ in Fig. 8. Other trajectories produce unphysical behaviors of radius and mass flow (Fig. 9).

As a practical matter, for propellants with $n > 1/2$ it is essentially impossible to begin the integration of (43) and (44) at $(U, V) = (0, 0)$, or even close to it, because of the instability of neighboring trajectories. Instead, the sign of the integration parameter α is reversed, effectively reversing the direction arrows on the phase plane. The initial coordinates for the integration are chosen very close to the saddle with a small initial displacement along the (now diverging) eigenvector directed toward the origin. With the integration stabilized in this way, the solution trajectory is easily determined, a process called exact shooting. Propellants with $n < 1/2$ are much easier since the trajectories near the origin (typified by the phase plane in Fig. 8b) are unstable (diverge from the origin) and all converge to the critical point.

6 Solution in limit $\theta \to 0$

According to (36), the initial condition $J(0) = 1$ implies the limit

$$\lim_{\theta\to 0} v(\theta) = \theta^{2n-2m+1}. \tag{50}$$

The dimensionless regression rate equation in the limit $\chi \to 0$ is

$$\lim_{\chi\to 0} \frac{\partial R(\chi,\tau)}{\partial \tau} = \frac{1}{\chi^m R^{2n}}, \tag{51}$$

which integrates to

$$\lim_{\chi\to 0} R(\chi,\tau) = (2n+1)^{\frac{1}{2n+1}}\left(\frac{\tau}{\chi^m}\right)^{\frac{1}{2n+1}}. \tag{52}$$

Equation (52) can be recast in similarity variables. From (29)

$$\lim_{\theta\to 0} K(\theta) = (2n+1)^{\frac{1}{2n+1}} \left(\frac{1}{\theta^{\left(\frac{2n-2m+1}{(2n-1)(2n+1)}\right)}} \right), \tag{53}$$

and using (36)

$$\lim_{\theta\to 0} u(\theta) = \frac{\theta^{\left(\frac{n}{2n+1}\right)(2n-2m+1)}}{(2n+1)^{\frac{1}{2n+1}}}. \tag{54}$$

The variable θ in the limits (50) and (54) can be eliminated to produce the relationship between $u(\theta)$ and $v(\theta)$ near the critical point at $(u_c, v_c) = (0, 0)$, where $\theta \to 0$.

$$\lim_{(u,v)\to(0,0)} v(u) = (2n+1)^{\frac{1}{n}} u^{\frac{2n+1}{n}}. \tag{55}$$

Notice that at the critical point $(u_c, v_c) = \left((2n-2m+1)^n (1-n)^{1-n}, (2n-2m+1)^{2n+1}/(1-n)^{(2n-1)}\right)$, u and v are related by

$$v_c = \frac{1}{(1-n)^{\frac{1}{n}}} u_c^{\frac{2n+1}{n}}, \tag{56}$$

i.e., by the *same* power of u as the solution near $\theta \to 0$ (55). In normalized variables we have the limits

$$\lim_{\theta\to 0} U(\theta) = \frac{\theta^{\left(\frac{n}{2n+1}\right)(2n-2m+1)}}{(2n-2m+1)^n (1-n)^{1-n} (2n+1)^{\frac{1}{2n+1}}}, \tag{57}$$

$$\lim_{\theta\to 0} V(\theta) = \frac{(1-n)^{(2n-1)}}{(2n-2m+1)^{2n+1}} \theta^{(2n-2m+1)}, \tag{58}$$

$$\lim_{(U,V)\to(0,0)} V(U) = (1-n)^{\frac{1}{n}} (2n+1)^{\frac{1}{n}} U^{\left(\frac{2n+1}{n}\right)}, \tag{59}$$

$$\lim_{(U,V)\to(1,1)} V(U) = U^{\frac{2n+1}{n}}. \tag{60}$$

7 Approximate solution for $V(U)$

In lieu of an analytical solution of (46), we can take advantage of the common exponent connecting (59) and (60) to come up with a useful approximation to $V(U)$ in the range $0 < U < 1$.

$$\text{Let } V = \left(U^2 + (1-n)^{\frac{1}{n}} (2n+1)^{\frac{1}{n}} \left(1 - U^2 g(n,U)\right)\right) U^{\frac{2n+1}{n}}, \tag{61}$$

where $g(n, U)$ is numerically determined to minimize the error in the solution of (46). For example, the choice $g(n, U) = 1$ captures $V(U)$ quite well, especially near $U = 0$. An equivalent form is

$$V = k(n)\left(1 + \left(\frac{1-k(n)}{k(n)}\right) U^2 g(n,U)\right) U^{\frac{2n+1}{n}}, \tag{62}$$

where

$$k(n) = (2n+1)^{\frac{1}{n}} (1-n)^{\frac{1}{n}} \tag{63}$$

is plotted in Fig. 10.

In Fig. 11a, approximation (62) with $g(n, U) = 1$ is plotted against the exact-shooting numerical integration of (46). The coincidence of these curves is so close that (62) had to be shifted upward so it could be distinguished. However, the derivatives derived from (62) and the exact-shooting solution shown in Fig. 11b do deviate slightly

Fig. 10 The function $k(n)$

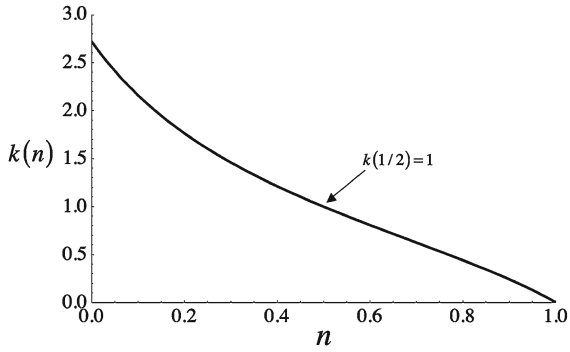

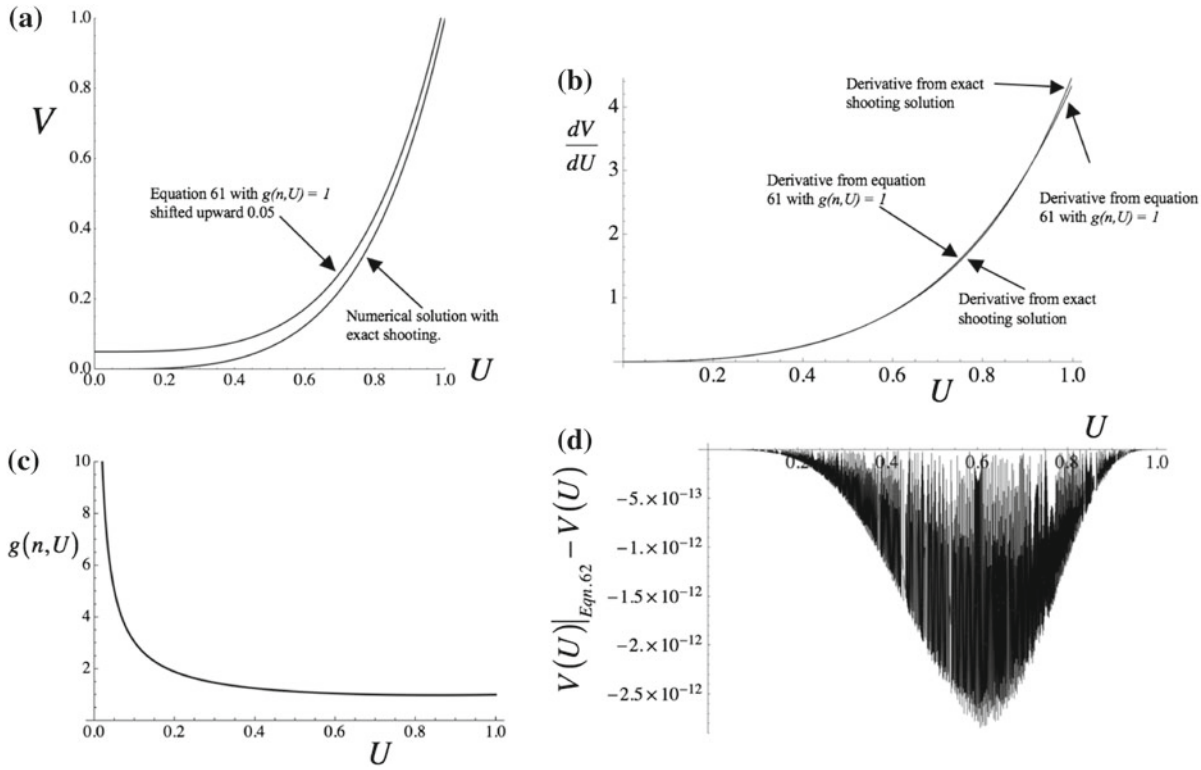

Fig. 11 Comparison between "exact" numerical solution of (46) and approximation (62) for $n = 0.8$. **a** $V(U)$ with g = 1. **b** dV/dU with g = 1. **c** $g(n,U)$ for high accuracy. **d** Difference between Eq. (62) with $g(n,U)$ as in **c** and the exact-shooting solution

near the critical point. This is a problem when it comes to integrating the mass transfer along the port to determine the O/F ratio. Small errors in the derivative accumulate, making the $g(n, U) = 1$ approximation too crude to determine this important variable. Instead, it is necessary to determine $g(n, U)$ so that the $V(U)$ given by (62) is a very accurate approximation to the solution generated by exact shooting. A typical result for $n = 0.8$ is illustrated in Fig. 11c and d.

The initial values of the solution, U_0 and θ_0, are chosen to be sufficiently small so that they are accurately related by the solution near the origin:

$$U_0 = \frac{\theta_0^{\left(\frac{n}{2n+1}\right)(2n-2m+1)}}{(2n-2m+1)^n(1-n)^{(1-n)}(2n+1)^{\frac{1}{2n+1}}}. \tag{64}$$

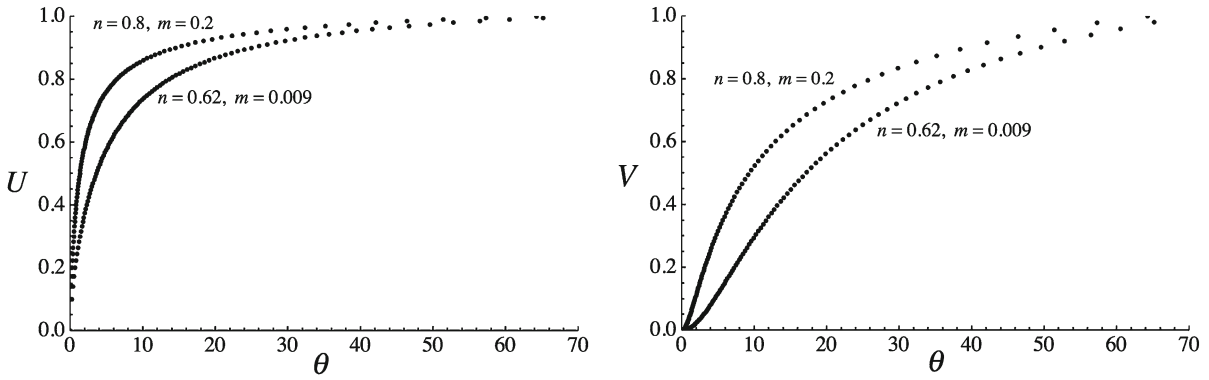

Fig. 12 Functions $U(\theta)$ and $V(\theta)$ from (65) and (66) for two cases

8 Numerical solution for $U(\theta)$ and $V(\theta)$ using (62) and (64)

Integrate (43) using (62) and (39):

$$\mathrm{Log}\left(\frac{\theta}{\theta_0}\right) = \int_{U_0}^{U} \left(\frac{k^n \left(1 + \left(\frac{1-k}{k}\right) \tilde{U}^2 g\left(n, \tilde{U}\right)\right)^n}{\left(\left(\frac{1-n}{2n-1}\right)(2n-2m+1)\right) \tilde{U} \left(1 - k^n \left(1 + \left(\frac{1-k}{k}\right) \tilde{U}^2 g\left(n, \tilde{U}\right)\right)^n\right)} \right) \mathrm{d}\tilde{U}, \tag{65}$$

where U_0 and θ_0 are related by (64). The integral (65) generates $U(\theta)$. The singularity at $\theta = 0$ is not really a problem since one can begin the numerical integration of (65) at a very small but finite U_0, with θ_0 determined from (64). Once $U(\theta)$ is determined, then $V(\theta)$ is found from (62), expressed as

$$V(\theta) = k\left(1 + \left(\frac{1-k}{k}\right) U(\theta)^2 g(n, U(\theta))\right) U(\theta)^{\frac{2n+1}{n}}. \tag{66}$$

Results for the classic case $(n, m) = (0.8, 0.2)$ and paraffin fuel burning with oxygen $(n, m) = (0.62, 0.009)$ are shown in Fig. 12.

An interpolation function is fit to the data generated by (65) and (66) (10^4 points), and from then on $U(\theta)$ and $V(\theta)$ are treated as known solutions of (42) and (43).

9 Solution expressed in space–time variables

Finally, the solutions discussed previously can be recast in terms of the original dimensionless space–time variables using (36) and (29). The full solution is

$$R = \frac{\tau^{1-n} \chi^{n-m}}{(2n-2m+1)^n (1-n)^{1-n} U(\theta)}, \tag{67}$$

$$J = \frac{(1-n)^{(2n-1)} \chi^{(2n-2m+1)}}{(2n-2m+1)^{2n+1} \tau^{(2n-1)} V(\theta)}. \tag{68}$$

Recall $\theta = \chi/\tau^{\left(\frac{2n-1}{2n-2m+1}\right)}$ and $k = (2n+1)^{\frac{1}{n}}(1-n)^{\frac{1}{n}}$. At the critical point $\theta \to \infty$, where $(U, V) = (1, 1)$, the solution is

$$R = \frac{\tau^{1-n} \chi^{n-m}}{(2n-2m+1)^n (1-n)^{1-n}}, \tag{69}$$

$$J = \frac{(1-n)^{(2n-1)} \chi^{(2n-2m+1)}}{(2n-2m+1)^{2n+1} \tau^{(2n-1)}}. \tag{70}$$

Functions (69) and (70) exactly satisfy the original system of PDEs (19) and (20).

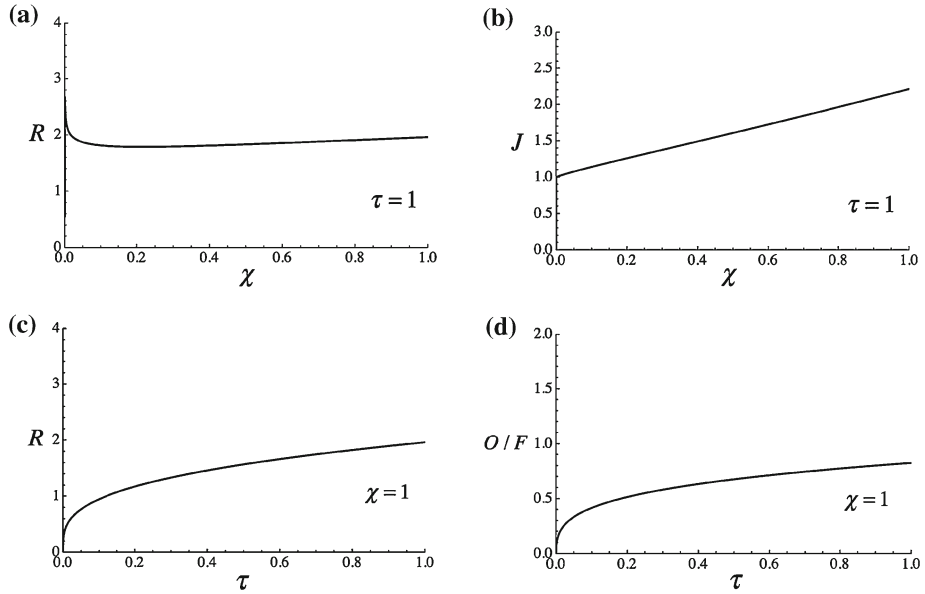

Fig. 13 **a, b** Radius and mass flow along port for $n = 0.8$, $m = 0.2$ at time $\tau = 1$. **c, d** Radius and O/F evolution at $\chi = 1$

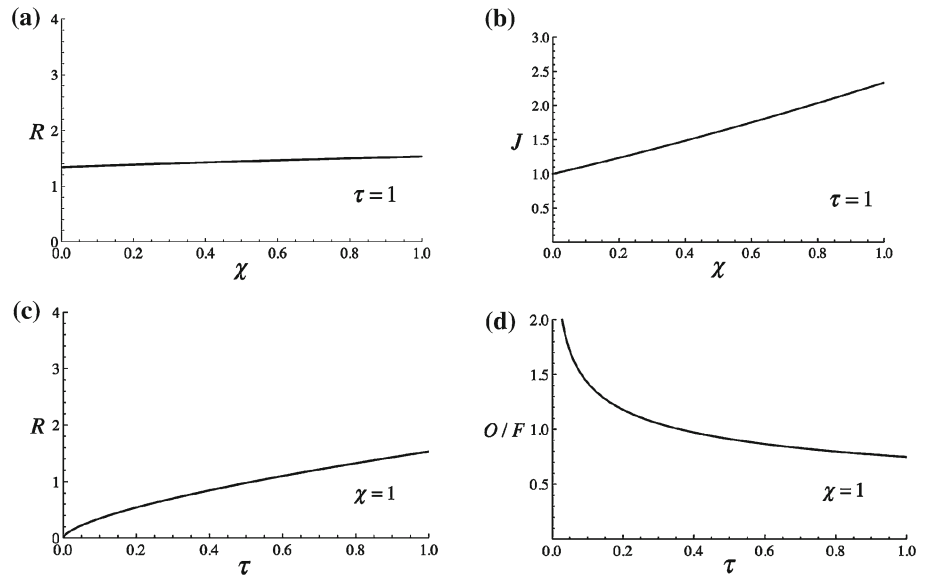

Fig. 14 **a, b** Radius and mass flow along the port for $n = 0.3$, $m = 0.0$ at time $\tau = 1$. **c, d** Radius and O/F time evolution at end of port, $\chi = 1$

10 Dimensionless radius and mass flow solutions

Examples of the solution of (67) and (68) are shown in Figs. 13 and 14 below. A couple of features of these plots are worth noting. The first is the singularity in port radius at $\chi = 0$ for the$(n, m) = (0.8, 0.2)$ case. This comes from the dependence of the regression rate on χ^{-m} in Eq. (19), producing an infinite regression rate at the origin. This harks back to the original formulation by Marxman and the relationship of the mass transfer rate to skin friction, which is infinite at $x = 0$. For the mass flow, the singularity in Eq. (20) cancels and the boundary condition $J(0) = 1$ is satisfied.

The singularity in the radius at $\chi = 0$ is gone when m is set to zero for the $n < 1/2$ case shown in Fig. 14. The time evolution of the flow at $\chi = 1$ is also shown; in both cases the port radius increases monotonically from zero, as one would expect.

Figures 13d and 14d show the time variation of the O/F ratio. Recall that $J = (\dot{m}_{ox} + \dot{m}_f)/\dot{m}_{ox} = 1 + 1/(O/F)$. For $n > 1/2$ the amount of fuel generated along the port decreases with time as the port opens up. As noted earlier, this is because the decrease in mass flux dominates the increase in port surface area, as suggested by the simplified O/F Eq. (4) discussed in the introduction. As a consequence, the O/F increases monotonically with time at $\chi = 1$. For $n < 1/2$ the opposite occurs.

For $m > 0$ the port radius has a minimum near the entrance, then increases monotonically along the port. For $m = 0$ there is no minimum. While the increase in $R(\chi)$ along the port is relatively gentle, to a designer it is not a desirable feature because it implies that there may be a significant unburned sliver of fuel at the end of the burn. This is because the motor must be throttled off when the combustion reaches the motor case to prevent a burn-through.

Another feature of these examples is that the aspect ratio of the port (port length/port radius, L_{port}/r) is relatively small. The port is too short to be a practical motor since much of the oxidizer could not be burned before leaving the port. Another problem is that in the $n = 0.3$ example the mass flow at the end of the port implies an impractically low O/F ratio, too low to be relevant to any realistic oxidizer–fuel combination.

To look more deeply into the design problem, we need to work out time, length, and mass scales for a real problem and analyze a couple of dimensioned examples.

11 Dimensioned radius and mass flow solution, matter of scaling

For convenience, the scale relations (16) are repeated here:

$$T_{ch} = \left[\frac{(\dot{m}_{ox})^{\frac{1-n+m}{2-2n-m}}}{(\pi^{-n} a)^{\frac{3}{2-2n-m}} (2\pi\rho_f)^{\frac{1+2n+m}{2-2n-m}}} \right],$$

$$L_{ch} = \left[\frac{(\dot{m}_{ox})^{\frac{1-n}{2-2n-m}}}{(\pi^{-n} a)^{\frac{1}{2-2n-m}} (2\pi\rho_f)^{\frac{1}{2-2n-m}}} \right], \tag{71}$$

$$M_{ch} = \left[\frac{(\dot{m}_{ox})^{\frac{3-3n}{2-2n-m}}}{(\pi^{-n} a)^{\frac{3}{2-2n-m}} (2\pi\rho_f)^{\frac{1+2n+m}{2-2n-m}}} \right].$$

The table below shows data for several commonly used propellant combinations. Data for a and n for a variety of fuels can be found in Zilliac and Karabeyoglu [19] and Doran et al. [20]. The initials HDPE refer to high-density polyethylene. The most striking feature of Table 1 is the very large values of T_{ch} driven by the small values of the regression rate constant a. The dependence of the time scale expression in (71) on a is

Table 1 Regression rate data for commonly used propellants

Fuel/oxidizer	Paraffin/O_2	HDPE/O_2	HDPE/N_2O
$\rho_f \times 10^{-3}$	0.920	0.941	0.941
n	0.62	0.498	0.331
m	0.009	0.0	0.0
$a \times 10^5$	9.240	4.193	11.573
$T_{ch}/(\dot{m}_{ox})^{\frac{1-n+m}{2-2n-m}} \times 10^{-6}$	1.206	2.095	0.03237
$L_{ch}/(\dot{m}_{ox})^{\frac{1-n}{2-2n-m}}$	5.931	7.077	1.763
$M_{ch}/(\dot{m}_{ox})^{\frac{3-3n}{2-2n-m}} \times 10^{-6}$	1.206	2.095	0.03237

Dimensioned data are in mks units

$$T_{\rm ch}\left(2\pi\rho_f\right)^{\frac{1+2n+m}{2-2n-m}} / \left(\dot{m}_{\rm ox}\right)^{\frac{1-n+m}{2-2n-m}} = \left[1/\left(\frac{a}{\pi^n}\right)^{\frac{3}{2-2n-m}}\right]. \tag{72}$$

The strong dependence of the exponent $3/(2-2n-m)$ on n, especially for values of n approaching one, makes the time scale very sensitive to both a and n. Sensitivity of this exponent to the oxidizer mass flow rate is less because of the factor $1-n$ that appears in the numerator of the exponent in each scale. Fuel density variations are relatively small for the solid hydrocarbons that are normally used in hybrid propulsion, and most have a specific gravity around one. The length exponents m for HDPE are set to zero in Table 1 not because they are known to be zero but because of the absence of adequate data in the literature. Despite the odd magnitudes, these are the appropriate scales for hybrid rockets. The characteristic time is on the order of the time it would take for the combustion to consume a cylindrical fuel grain of radius $L_{\rm ch}$, and the characteristic mass is the total oxidizer mass consumed in the process. The process takes so long because the mass flux in the port decreases to extremely low levels as the port opens up.

In practice, typical rocket burn times vary from a few seconds to perhaps as much as a few hundred seconds. The implication of the time scale data in Table 1 is that for all practical purposes the value of τ for a real motor tends to be very small, typically $\tau < 10^{-4}$. To see the impact of this, let us examine two specific cases.

Case 1 – Paraffin burning with oxygen $(n, m) = (0.62, 0.009)$.

Set the oxidizer mass flow rate to $\dot{m}_{\rm ox} = 4.43\,{\rm kg/s}$. Characteristic scales for this case are

$$T_{\rm ch} = 2.607 \times 10^6\,{\rm s}, \quad L_{\rm ch} = 12.594\,{\rm m}, \quad M_{\rm ch} = 1.155 \times 10^7\,{\rm kg}. \tag{73}$$

Take the port length to be $L_{\rm port} = 1.149\,{\rm m}$. The initial and final burn times are $t_{\rm burn1} = 4.20\,{\rm s}$ and $t_{\rm burn2} = 12.45\,{\rm s}$. For these burn times, $\tau_{\max 1} = 1.611 \times 10^{-6}$ and $\tau_{\max 2} = 4.776 \times 10^{-6}$.

Several features are apparent in these results. The immediate effect of the nonzero exponent m is to produce a singularity in the radius at $x = 0$, which acts only over a very short distance (barely discernible in Fig. 15a). The residual effect is to produce a transition region over about the first 0.5% of the length of the port where the radius decreases slightly with x. The regression rate Eq. (19) suggests that the regression rate might decrease near the entrance of the port until the flux term in the numerator can overtake the distance term in the denominator. The mass flow J increases monotonically, as it should. The radius after this transition is remarkably constant, although not precisely so, and the amount of variation is important because it affects the degree to which all of the fuel can be consumed, as mentioned earlier. After the minimum radius point there is about a 6–9% increase in the port radius to the end of the port. This is called "coning" and is commonly seen in hybrids of this size. The near constancy of the port radius can be understood by recognizing that if a radius-reducing bump were to occur at some point along the port, there would be a corresponding local increase in the mass flux leading to a more rapid regression rate that would tend to smooth out the bump.

The solution shown in Fig. 15 is a similarity solution that begins with zero port radius, but it also applies exactly to an 8.25 s burn that begins with the $t = 4.20\,{\rm s}$ initial radius distribution shown in Fig. 15a. The fact that the initial radius is so nearly constant along the port suggests that it should also be applicable to a realistic situation where the initial port distribution is strictly constant with allowance for a short initial adjustment period. The example shown in Fig. 15 is chosen to correspond to case 4L-05 shown in Table 1 of Karabeyoglu et al. [12]. The data are reproduced in Table 2.

To be clear, the measured data in Table 2 were used by Karabeyoglu et al. [12], together with numerical integration of (8) and (9), to infer the values of n, m, and a in Table 1 for paraffin/LOx. The fact that the port radii and O/F ratio in column 3 of Table 2, derived from the similarity solution, match so well with the measured data indicates that the similarity solution accurately reproduces the full numerical solution of PDEs (19) and (20). The only minor difference is the higher percentage change between the fore and aft end of the port from the similarity solution. This is consistent with the fact that the initial port geometry in the similarity solution is slightly coned.

Looking back at the I_{sp} plot in Fig. 6 for paraffin/O_2 and comparing it with the O/F variation at the end of the port shown in Fig. 15d it can be noted that this design has achieved its main goal of operating in a range of O/F ratios close to the point of maximum I_{sp}. A further point that is worth noting but is a little outside the scope of this

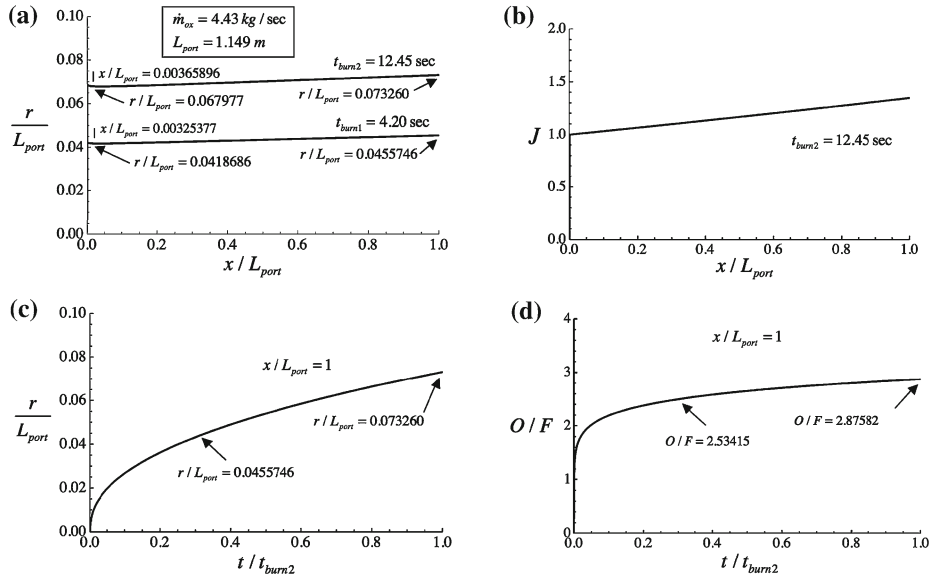

Fig. 15 Paraffin burning with oxygen $(n, m) = (0.62, 0.009)$. **a** Port radius as a function of x at end of initial and final burn. **b** Mass flow along port at end of final burn. **c, d** Radius and O/F evolution at end of port

Table 2 Measured port data and O/F ratio compared to similarity solution

Measured variable	Test 4L-05	Similarity solution (Fig. 15)
Oxidizer mass flow rate (kg/s)	4.43	4.43
Burn time (s)	8.25	8.25
Grain length (m)	1.149	1.149
Initial port radius (m)	0.05005	0.05005 (averaged along port)
Final port radius (fore end) (m)	0.0794	0.0783
Final port radius (aft end) (m)	0.0832	0.0842
Percentage increase in radius along port	4.79	7.54
Overall O/F ratio	2.72	2.73

paper is that the aspect ratio of the port is in the range $14 < L/r < 23$, a range that is geometrically consistent with the growth rate of the mass transfer, heat transfer-driven turbulent boundary layer along the port. This means that the oxidizer should be fully consumed at the end of the port. The port is not too short (unmixed oxidizer in the free stream) or too long (unreacted fuel leaving the port) but just about right. This motor should operate very well.

Case 2 – HDPE burning with nitrous oxide $(n, m) = (0.331, 0.0)$

The oxidizer mass flow rate is the same as in Case 1. Characteristic scales for this case are

$$T_{\text{ch}} = 6.8140 \times 10^4\ \text{s} \quad L_{\text{ch}} = 3.7098\ \text{m} \quad M_{\text{ch}} = 3.0186 \times 10^5\ \text{kg}. \tag{74}$$

The port length and burn times also remain the same as in Case 1. For this example $\tau_{\max 1} = 6.1638 \times 10^{-5}$ and $\tau_{\max 2} = 18.2711 \times 10^{-5}$; both are considerably larger than in Case 1.

With $m = 0$ the port radius increases monotonically along the port, and for $n < 0.5$ the port is almost straight, changing by less than 1%. The most significant feature in the solution is the very large aspect ratio of the port with $40 < L/r < 77$ over the course of the burn. The O/F ratio in Fig. 16d is too high by a factor of three for this propellant combination for which the maximum I_{sp} would actually occur at approximately $O/F = 6$. This port is much too short, a consequence of the low regression rate of HDPE and the main reason hybrids using polymeric fuels must use a multiport design.

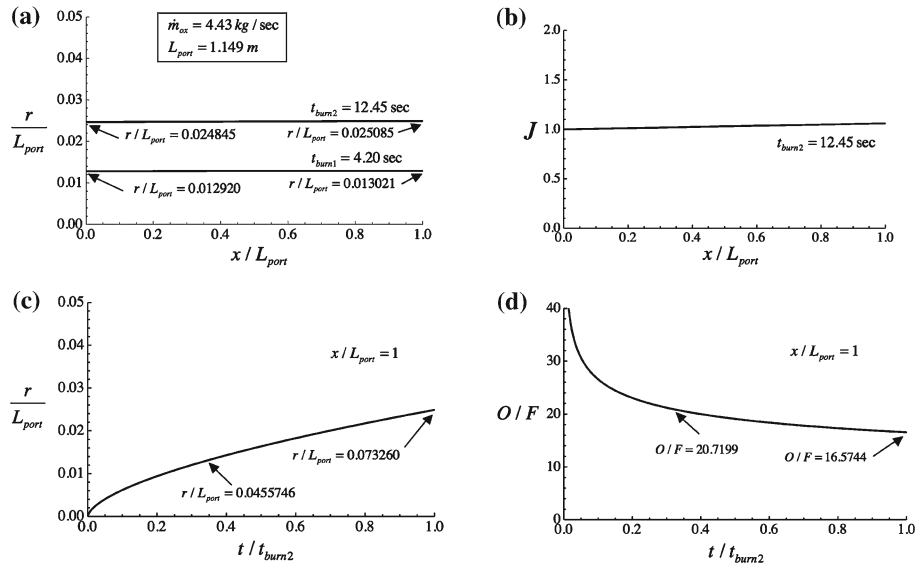

Fig. 16 HDPE burning with nitrous oxide $(n, m) = (0.331, 0.0)$. **a** Port radius as a function of x at end of initial and final burn. **b** Mass flow along port at end of final burn. **c, d** Radius and O/F evolution at end of port

12 Concluding remarks

One of the most challenging problems in hybrid rocket design is the uncertainty in the regression rate law. The assumptions about the physics underlying Marxman's theory are necessarily simplified and little is really known about the mixing and combustion process inside a hybrid rocket where pressures are high and gas temperatures can exceed 3000 K. A first step at directly viewing the combustion was taken recently by Chandler [21] and Chandler et al. [22], but quantitative measurements are still in the future.

The fact is that the basic regression rate law (1) is known to work pretty well for a wide variety of propellants and a wide range of motor sizes. Nevertheless, considerable uncertainty surrounds the correct values of a, n, and m for a given propellant combination. For example, Table 2 in the paper by Zilliac and Karabeyoglu [19] has three sets of values $-(a, n) = \left(3.04 \times 10^{-5}, 0.681\right)$, $(a, n) = \left(9.03 \times 10^{-5}, 0.527\right)$, $(a, n) = \left(4.15 \times 10^{-5}, 0.670\right)$ – with $m = 0$ from three different sources for the widely used fuel hydroxyl-terminated polybutadiene (HTPB) burning with oxygen. Boardman et al. [23] studied the HTPB/oxygen system and introduced the regression rate law:

$$\bar{\dot{r}} = 0.065 \bar{G}_{\mathrm{ox}}^{0.77} \left(\frac{\bar{D}_p}{3} \right)^{0.71}, \tag{75}$$

where the overbar refers to a time–space average and the factor involving D_p is included to account for the effect observed in their data of average port diameter on the regression rate. They express the regression rate law in terms of temporally and spatially averaged quantities that are directly measurable. The average regression rate is determined from the initial and final space-averaged port diameters and the burn time. The average mass flux is typically based only on the oxidizer flow rate, which is a known test quantity.

This is by far the most common approach to inferring the regression rate law from test data. The effect of fuel mass flow on the regression rate is often ignored because it is so difficult to measure directly. Although X-ray measurements of the fuel regression rate have been made, as in the work of Evans et al. [24], the vast majority of regression rate data is based solely on measurements of the fuel grain before and after a test combined with oxidizer mass flow rate and chamber pressure measurements. Often papers are published without even including these key data.

The similarity solution presented here may provide a new approach to this problem that will allow globally averaged data to be used to infer the values of a, n, and m that produced the data. It remains to be seen whether or not this inverse problem can be solved uniquely. This was done numerically by Karabeyoglu et al. [12], and the results were quite promising. The similarity solution derived here may enable this approach to be used to help correlate the large body of averaged data that exists in the literature and improve our understanding of scale effects in hybrid design.

The similarity solution presented in this paper, combined with a suitable model of the growth rate of the combustion boundary layer, can be a useful starting point for the design of a hybrid propulsion system. Applications cover a wide range of scales, from small thrusters for spacecraft to large boosters for satellite launch, and the solution is a useful starting point for incorporating the effects of motor size and other run variables into the accurate prediction of fuel regression rate so important to satisfactory design.

Acknowledgments This work was supported by a Strategic University Research Partnership (SURP) grant from the Caltech–NASA Jet Propulsion Laboratory. My thanks to Stanford graduate student and NASA Ames researcher Laura Simurda, who helped proofread the manuscript.

References

1. Chiaverini MJ, Kuo KK (2007) Fundamentals of hybrid rocket combustion and propulsion, progress in astronautics and aeronautics vol 218, AIAA, Reston, Virginia
2. Marxman GA, Gilbert M (1963) Turbulent boundary layer combustion in the hybrid rocket, 9th international symposium on combustion, The Combustion Institute, Pittsburgh, PA, pp 371–383
3. Marxman GA, Wooldridge CE, Muzzy RJ (1964) Fundamentals of hybrid boundary layer combustion, heterogeneous combustion. In: Wolfhard HG, Glassman I, Green L Jr (eds) Progress in astronautics and aeronautics volume 15. Academic Press, New York, pp 485–521
4. Karabeyoglu MA, Altman D, Cantwell BJ (2002) Combustion of liquefying hybrid propellants: Part I general theory. AIAA J Propuls Power 18(3):610–620
5. Karabeyoglu MA, Cantwell BJ (2002) Combustion of liquefying hybrid propellants: Part II stability of liquid films under strong blowing. AIAA J Propuls Power 18(3):621–630
6. Benjamin TB (1959) Shearing flow over a wavy boundary. J Fluid Mech 6:161–205
7. Craik ADD (1966) Wind-generated waves in thin liquid films. J Fluid Mech 26:369–392
8. Gater RA, L'Ecuyer MR (1970) A fundamental investigation of the phenomena that characterize liquid film cooling. Int J Heat Mass Transf 13:1925–1939
9. Cantwell BJ, Karabeyoglu MA, Altman D (2010) Recent advances in hybrid propulsion. Int J Energ Material Chem Propuls 9(4):305–326
10. Marxman GA, (1967) Boundary layer combustion in propulsion, 11th international symposium on combustion, The Combustion Institute, pp 269–289
11. Karabeyoglu MA, Zilliac G, Cantwell BJ, DeZilwa S, Castellucci P (2004) Scale-up tests of high regression rate paraffin-based hybrid rocket fuels. AIAA J Propuls Power 20(6):1037–1045
12. Karabeyoglu MA, Cantwell BJ, Zilliac G (2005) Development of scalable space-time averaged regression rate expressions for hybrid rockets, AIAA 2005–3544, 41st Joint Propulsion Conference, p 1–21
13. Wooldridge CE, Muzzy RJ (1965) Measurements in a turbulent boundary layer with porous wall injection and combustion, 10th international symposium on combustion, The Combustion Institute, pp 1351–1362
14. Paul PJ, Mukunda HS, Jain VK (1982) Regression rates in boundary layer combustion, 19th international symposium on combustion, The Combustion Institute, pp 717–729
15. Olver P (1986) Applications of lie groups to differential equations. Graduate texts in mathematics. Springer, New York
16. Bluman GW, Kumei S (1989) Symmetries and differential equations. Applied mathematical sciences 81. Springer, New York
17. Ibragimov N (1998) Elementary lie group analysis and ordinary differential equations. Wiley, New York
18. Cantwell BJ (2002) Introduction to symmetry analysis. Cambridge Press, Cambridge Texts in Applied Mathematics
19. Zilliac G, Karabeyoglu MA (2006) Hybrid rocket fuel regression rate data and modeling, AIAA 2006–4504, 42nd Joint Propulsion Conference, pp 1–21
20. Doran E, Dyer J, Lohner K, Dunn Z, Cantwell B, Zilliac G (2007) Nitrous oxide hybrid rocket motor fuel regression rate characterization, AIAA 2007–5352, 43rd AIAA Joint Propulsion Conference, pp 1–12
21. Chandler A (2012) An investigation of liquifying liquefying hybrid rocket fuels with applications to solar system exploration, PhD thesis Stanford University, Palo Alto, CA

22. Chandler A, Jens ET, Cantwell BJ, Hubbard GS (2012) Visualization of the liquid layer combustion of paraffin fuel at elevated pressures, 63rd International Astronautical Congress. Naples, Italy
23. Boardman TA, Carpenter RL, Goldberg BE, Shaeffer CW (1993) Development and testing of 11 and 24 inch hybrid motors Under the Joint Government/Industry IR&D program, AIAA 93–2552, 29th Joint Propulsion Conference, pp 1–24
24. Evans B, Risha GA, Favorito N, Boyer E, Wehrman RB, Libis N, Kuo KK (2003) Instantaneous regression rate determination of a cylindrical X-ray transparent hybrid rocket motor, AIAA 2003–4592, 39th Joint Propulsion Conference, pp 1–11